Noncontact Viscoelastic Imaging of Living Cells Using a Long-Needle Atomic Force Microscope with Dual-Frequency Modulation

Dongshi Guan,[1] Elisabeth Charlaix,[2] Robert Z. Qi,[3] and Penger Tong[1]
[1]*Department of Physics, Hong Kong University of Science and Technology, Clear Water Bay, Kowloon, Hong Kong*
[2]*LIPHY, Université Grenoble Alpes, F-38000 Grenoble, France*
[3]*Division of Life Science and State Key Laboratory of Molecular Neuroscience, Hong Kong University of Science and Technology, Clear Water Bay, Kowloon, Hong Kong*
(Received 23 April 2017; revised manuscript received 26 July 2017; published 20 October 2017)

Imaging of surface topography and elasticity of living cells can provide insight into the roles played by the cells' volumetric and mechanical properties and their response to external forces in regulating the essential cellular events and functions. Here, we report a unique technique of noncontact viscoelastic imaging of live cells using atomic force microscopy (AFM) with a long-needle glass probe. Because only the probe tip is placed in a liquid medium near the cell surface, the AFM cantilever in air functions well under dual-frequency modulation, retaining its high-quality resonant modes. The probe tip interacts with the cell surface through a minute hydrodynamic flow in the nanometer-thin gap region between them without physical contact. Quantitative measurements of the cell height, volume, and Young's modulus are conducted simultaneously. The experiment demonstrates that the long-needle AFM has a wide range of applications in the study of cell mechanics.

DOI: 10.1103/PhysRevApplied.8.044010

I. INTRODUCTION

Mechanical stresses and response of living cells to the resulting deformations play important roles in cell contraction, spreading, crawling, wound healing, invasion, and division [1–6]. Many aspects of a cell's motility, differentiation, and cancerization are also governed by the stress and elasticity of its surroundings [7–14]. Understanding the microscopic origin of the mechanical properties of the cell and its relation to the underlying cell structure and response is, therefore, essential to mechanobiology. For these reasons, the past decades have witnessed a growing interest in developing various novel techniques to measure the viscoelastic property of living cells ranging from micropipette aspiration [15,16], microplate manipulation [17], and colloidal probe indentation [18,19] to magnetic and optical tweezers [20,21], and microrheological methods based on single particle tracking [22,23]. Among these methods, atomic force microscopy (AFM) techniques have served as an effective and versatile platform for both the high-resolution imaging of a cell's surface topography and the measurement of forces and elasticity of living cells [24–27]. They have been used to study a wide range of problems in cell biology, such as a cell's adhesion, locomotion, differentiation, division and shape, cytoskeleton remodeling, and tissue development [7,8,25,26,28–35].

Although considerable progress has been made in recent years to develop various techniques to measure the mechanical property of living cells, the current technology still faces many challenges and has considerable limitations in accurately determining the elastic modulus of either very thin films or very soft materials, such as live cells. For example, the Young's modulus E of living cells measured by different techniques varies by 3 orders of magnitude from 0.1 to 100 kPa [26]. This is caused by several reasons. First, the theoretical models that are used to calculate E are often oversimplified with assumptions that barely approximate the actual geometry and complex structure of live cells. An accurate determination of cell elasticity requires a reliable model, which can accommodate the actual measurement geometry. Second, many of the advanced AFM techniques, such as frequency modulation and dual-frequency imaging [36,37], are originally designed for operation in air and do not function well in a liquid environment for a biology experiment [38]. The motion of the AFM cantilever is severely damped by the fluid viscosity, and the piezoelectric shaker used to drive the cantilever also generates unwanted flow modes near the probed surface. As a result, the AFM imaging and force measurement for live cells become difficult and time consuming and require extensive working experience and a great deal of patience [26]. Finally, as will be shown below, living cells have a heterogeneous surface and their elasticity varies significantly among different locations of the cell and at different stages of the cell cycle. Therefore, an imaging method is needed in order to have a spatially resolved elasticity map of live cells. In addition, as the living cells are rather soft and delicate, a strong direct forcing on the plasma membrane and cytoskeleton cortex with a sharp tip may penetrate through the membrane, causing cell damage and probe contamination during the mechanical measurement [23,39,40].

In this paper, we report a unique design of "long-needle" AFM under dual-frequency modulation with one being the standard light tapping for surface topography and the other being frequency locked at resonance for viscoelastic mapping. This AFM setup combined with the newly developed linear elastohydrodynamic (EHD) theory [41,42] overcome the experimental difficulties mentioned above and provide a sensitive and versatile imaging tool for simultaneous noncontact measurements of cell height (topography), volume, and spatial distribution of the Young's modulus of living cells. Our experiment verifies the technique and demonstrates its applications. This work thus may lead to the study of a range of interesting phenomena in cell mechanics with nanoscale resolution.

II. WORKING PRINCIPLE OF THE LONG-NEEDLE AFM

Figure 1 shows how the long-needle AFM works for noncontact mechanical measurement of living cells in a liquid medium. The long-needle probe consists of a long vertical glass fiber with one end glued onto the front end of a cantilever beam and the other end immersed through a thin liquid layer. The overall dimension of the glass fiber is designed with fiber length $\ell = 100$–200 μm, diameter $d = 1$–3 μm, and tip radius $R = 50$–1000 nm. With this design, the cantilever functions well in air without introducing extra disturbances to the system and the overall viscous damping ξ on the long needle is minimized [38,43–45].

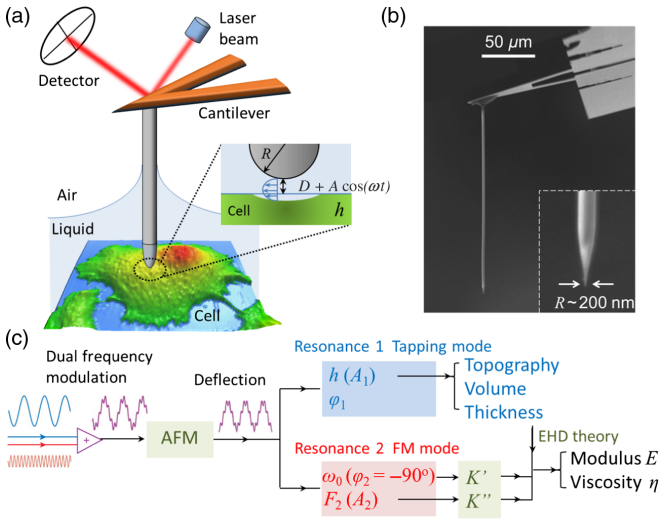

FIG. 1. Schematic of the system. (a) Sketch of the experimental setup. The inset shows the flow geometry in the gap region between the fiber tip and cell surface. (b) A scanning electron microscope image of the actual long glass fiber of diameter $d \simeq 2.5$ μm and length $\ell \simeq 180$ μm. The inset shows a magnified image of the fiber tip with radius $R \simeq 200$ nm. (c) A flowchart showing the AFM controls for simultaneous topographic and viscoelastic mapping with dual-frequency modulation (see text for more details).

Figure S1 in the Supplemental Material [46] shows the first two resonant modes of the long-needle cantilever. The values of the quality factor Q of the first two resonant modes are, respectively, 10 and 35, which are much larger than the typical Q value (2 to 4) for the same type of cantilever fully immersed in a liquid, which is used in the conventional method. As a result, the modified cantilever can still retain its high-quality resonant modes when the fiber tip is placed near the cell surface in a liquid medium. A thin layer of poly(L-lysine)-graft-poly(ethylene glycol) is coated on the glass fiber, which effectively reduces the contact line pinning at the liquid interface and provides a high degree of resistance to protein adsorption on the fiber in contact with a culture medium [49].

The living cells cultured on a coverslip are placed in an AFM fluid chamber (see Fig. S5). The thickness of the liquid layer above the coverslip is controlled in the range of 50–100 μm by using two syringe pumps (LSP02-1B, Longer) for suction and infusion, respectively. The AFM cantilever holder is mounted on the top of the chamber, which is covered by a flexible rubber diaphragm to minimize the evaporation of liquid inside the chamber. There is an extra hole on the sidewall of the chamber (pointed to by an arrow), which is used for slow infusion of a humidified gas mixture of 95% air and 5% CO_2.

The AFM is operated under the dual-frequency modulation mode, as sketched in Fig. 1(c). Two driving signals with different frequencies (blue and red signals) are used to simultaneously excite two independent vertical oscillation modes of the cantilever. In this case, the fiber tip is oscillated with the same frequencies at a distance D away from the cell surface and interacts with the cell through the hydrodynamic flow, as shown in the inset of Fig. 1(a). The first driving signal is used for the standard tapping mode with its frequency fixed near the first resonance of the cantilever. Under the tapping mode (blue box), the oscillation amplitude A_1 is kept at the set-point value by adjusting the cantilever's vertical position $h(A_1)$, which provides the surface topography of the cell and the precise value of the cell height. From the measured h, one can accurately calculate the cell volume by integrating h over the occupied area of the cell.

The second driving signal is used for the frequency modulation (FM) mode with its frequency locked exactly at the second resonance of the cantilever. Under the FM mode (red box), the motion of the modified cantilever is well described by the equation [43,44,50],

$$m\ddot{z} + \xi\dot{z} + k_c z = F_2 \cos(\omega t) - f_h(D), \qquad (1)$$

where m is the effective mass of the modified cantilever, $\xi\dot{z}(t)$ is the drag force acting on the fiber with ξ being its friction coefficient, $k_c z$ is the elastic restoring force due to the bending of the cantilever with a spring constant k_c, $F_2 \cos(\omega t)$ is the driving force with amplitude F_2 and

angular frequency ω, and $-f_h(D)$ is the hydrodynamic reaction force on the needle tip resulting from deformations of the cell surface. With the EHD theory [41,42], one has $f_h(D) = K^*(D)z$, where $z(t) = A_2\cos(\omega t + \varphi_2)$ is the resulting tip oscillation, and $K^*(D) \equiv K'(D) + iK''(D)$ is the complex dynamic response function, which contains information about the elastic modulus E and viscosity η of the cell.

Under the FM mode, ω is continuously adjusted via a phase-lock loop to keep the modified cantilever at the *in situ* resonance with $\varphi_2 = -90°$. One can then solve Eq. (1) and obtain $\omega = \omega_0 = [(k_c + K')/m]^{1/2}$ and $F_2 = A_2(K'' + \xi\omega_0)$ (see Sec. II of the Supplemental Material [46] for more details). Another feedback loop is used to keep the oscillation amplitude A_2 at a constant set point (typically 1–2 nm) by varying F_2, so that one can obtain K' and K'', respectively, from the measured resonant frequency ω_0 and dissipative force F_2. In contrast, the phase φ_1 under the tapping mode contains convoluted information about K' and K'' and thus is not used in this experiment. The spacial resolution for the noncontact AFM imaging is determined by the lateral extension of the flow in the gap region, as sketched in the inset of Fig. 1(a). This region is of the order of $(2RD)^{1/2} \simeq 100$ nm for $D \simeq 10$ nm and $R \simeq 500$ nm [42,51], which are typical values used in the experiment. Similarly, the vertical impact region in the cell is also of the order of $(2RD)^{1/2} \simeq 100$ nm, which is large enough to sense the cortical network underneath the cell membrane. Because the size of this impact region is much smaller than the penetration length of the oscillatory flow (several micrometers) [44], it will oscillate together with the oscillatory flow without much time delay and thus the measured cell response is essentially its static value independent of the actual oscillation frequency ω used.

III. HYDRODYNAMIC RESPONSE OF LIVING CELLS

To demonstrate the working principle of the long-needle AFM and find an optimal working distance D for viscoelastic imaging, we first conduct the AFM measurements with varying values of D at a fixed location of the cell. The measurement is made at a constant speed u under the dual-frequency modulation mode. Figure 2 shows the simultaneously measured amplitude A_1 and phase φ_1 near the first resonance of the cantilever, resonant frequency f_0, and driving voltage V_0 at the second resonance of the cantilever, and the steady-state dc value of the cantilever deflection z as a function of surface separation D between the needle tip and cell surface. It is seen that all the monitored signals show sharp changes as the needle tip approaches the cell surface. In particular, we observe a sudden increase of the deflection z when A_1 becomes ~25% of its free amplitude at a far distance [see Figs. 2(a) and 2(e)]. This is caused by the fact that when the needle tip touches the cell surface, its elastic repulsion forces the cantilever to reverse its bending direction and the deflection z reveals a sharp rise as the z-axis piezoelectric motor goes down further. This upturn point is thus used to define the contact point $D = 0$. In the actual cell imaging, we use the amplitude A_1 as a feedback to control the tip-sample distance D. Typically, we set the feedback value of A_1 to be 4–6 nm, which is ~60% of the free amplitude, to ensure $D \simeq 10$ nm even for rough surfaces. In this way, the contact damage to the live cell during the viscoelastic imaging is minimized.

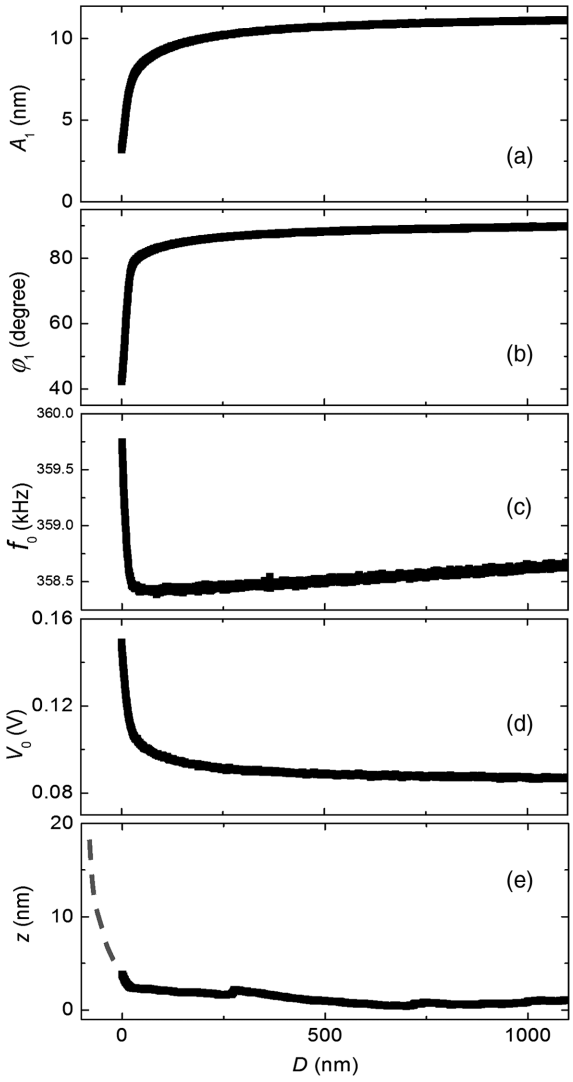

FIG. 2. Simultaneously measured (a) amplitude A_1, (b) phase φ_1, (c) resonant frequency f_0, (d) driving voltage V_0, and (e) deflection z of the AFM cantilever as a function of surface separation D between the needle tip and cell surface. The measurement is made with the needle tip approaching the cell surface at a constant speed $u = 100$ nm/s. The gray dashed line in (e) illustrates the traditional elastic measurement on living cells by a forced indentation.

The above procedure is well defined in the AFM tapping-mode operation, and the noncontact viscoelastic imaging referred in this paper is relative to the contact point $D = 0$, as defined above. For many cells, their surfaces are actually very rough with protrusions, such as microvilli, microridges, and other brushlike structures [52]. If these protrusions are so soft that they do not affect the value of the feedback signal A_1, then they are irrelevant to the viscoelastic imaging attempted here. If these protrusions are elastic, the value of the feedback signal A_1 will change when the needle tip approaches the protrusion surface. In this case, the z-axis piezoelectric motor is adjusted based on the measured amplitude A_1 during the imaging to keep the tip-cell distance D constant relative to the well-defined contact point. This feedback mechanism is essentially the same as that for the conventional tapping mode AFM, which is capable of imaging the morphology of elastically rough surfaces.

Figures 2(c) and 2(d) show the simultaneously measured resonant frequency f_0 and driving voltage V_0, which are obtained under the frequency modulation mode at the second resonant frequency of the AFM cantilever. Here, V_0 is connected to the driving force $F_2 = cV_0$, where c is a calibration constant of the electromagnetic actuator (iDrive, Asylum Research). The values of f_0 and F_2, which are independent of A_1 and φ_1 at the first resonance, are used to calculate the response function $K'(D)$ and $K''(D)$.

Figure 3 shows the measured $K'(D)$ and $K''(D)$ as a function of D for a living Hela cell. Here, we have subtracted out the small background contributions from the surrounding liquid and liquid-air interface above the needle tip [53]. These background contributions have been carefully studied in recent experiments [43,44,54,55].

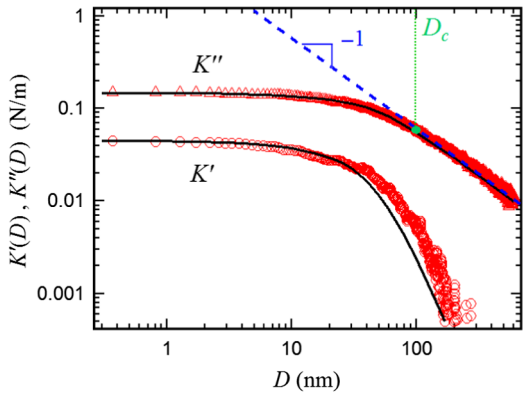

FIG. 3. Measured response function $K^*(D)$ for a living Hela cell. The real part $K'(D)$ (red circles) and imaginary part $K''(D)$ (red triangles) of $K^*(D)$ are obtained when a long-needle probe with tip radius $R = 355$ nm approaches the cell surface. The blue dashed line shows the Reynolds damping [Eq. (2)] for a rigid substrate, and the green dotted vertical line indicates the crossover distance $D_c \simeq 100$ nm. The black solid lines show the fits of the numerically calculated Eq. (3) to the data with the cell Young's modulus $E = 58 \pm 5$ kPa and viscosity $\eta = 11.9 \pm 2.4$ cP.

The measured $K^*(D)$ shows a sharp crossover behavior from an initial rapid increase with decreasing D for large D ($\gtrsim D_c$) followed by a plateau region with $D < D_c$. The crossover distance D_c is about 100 nm (green vertical dotted line). At large distance ($D \gtrsim D_c$), the fluid layer in the gap region is forced to drain in and out of the gap at the resonant frequency ω_0, generating a hydrodynamic pressure in the region. In this viscous regime, the response is dominated by the out-phase component,

$$K''(D) = \frac{6\pi\eta_0\omega_0 R^2}{D}, \tag{2}$$

which gives rise to the Reynolds damping force $F_h(D) \simeq K''(D)A_2$ between a (rigid) oscillating sphere and a rigid flat substrate [41,56]. Here, η_0 is the fluid viscosity and $F_h(D)$ is the amplitude of the reaction force $f_h(D)$. In this regime, the flow pressure $f_h(D)/2\pi RD$ is weak and does not indent the cell surface significantly. As a result, the real part $K'(D)$ is very small. As D decreases, the viscous pressure increases. When D becomes small enough ($D \ll D_c$), the cell surface cannot sustain the viscous pressure anymore and starts to deform and accommodate for most of the tip displacement A_2. In this "elastic regime," the fluid layer in the gap region is no longer expelled out of the gap, so that $K''(D)$ does not diverge as $1/D$. Instead, it saturates at a constant value K_0'' ($\simeq$0.15 N/m). If the cell surface were perfectly elastic, $K'(D)$ would be expected to eventually become larger than $K''(D)$ [41,42]. The fact that the measured $K_0' < K_0''$ suggests that the cell surface is viscoelastic.

The measured $K^*(D)$ can be well described by the linear EHD theory, which predicts that [41,42]

$$K^*(D) = i\frac{6\pi\eta_0\omega R^2}{D}\tilde{p}^*\left(\frac{D}{D_c};\alpha,\beta\right), \tag{3}$$

where $\tilde{p}^*(D/D_c;\alpha,\beta)$ is a dimensionless complex correction function due to the cell compliance. It contains two dimensionless mechanical parameters, $\alpha = (h/R)(E/\eta_0\omega)^{1/3}$ and $\beta = (h/R)(3\eta/\eta_0)^{1/3}$, which include the Young's modulus E, viscosity η, Poisson ratio ν, and height h of the cell. The numerically calculated Eq. (3) (black solid lines in Fig. 3) is found to fit the data well. There are two fitting parameters in Eq. (3), E and η, and the other parameters have been predetermined in the experiment (see Sec. III of the Supplemental Material [46] for more details).

In a previous experiment [53], the basic working principle of the long-needle AFM together with the EHD theory have been tested and verified using a standard polymer sample of polydimethylsiloxane (PDMS) thin films [53]. A consistent value of $E \simeq 600$ kPa was obtained for different values of the film thickness (250–900 nm) and fiber tip radius (800 and 220 nm). This value of E agrees

well with those obtained by other methods, such as the surface force apparatus [42] and centimeter-sized indenter [57]. Here, the obtained value of $E = 58 \pm 5$ kPa for the live Hela cell is at the high end of the modulus range obtained from other measurements [26]. This is probably caused by the fact that the stiffer cortical actin network underneath the cell membrane plays a dominant role in our AFM measurement, whereas the obtained values of E by other methods under a larger cell deformation contain more contributions from the softer cytoplasm inside the cell.

IV. ANALYTICAL EXPRESSION OF THE HYDRODYNAMIC RESPONSE FUNCTION $\tilde{p}(0;\alpha,\beta)$

To conduct noncontact viscoelastic measurement on living cells, we use the tapping mode to set the value of D in the elastic response regime ($\sim$10 nm) and measure the saturated values K_0' and K_0'' under the FM mode. Because of the fluid layer in the gap region, the needle tip is not in direct contact with the cell surface so that it will not penetrate through nor adhere to the cell membrane. Under light tapping, the amplitude A_1 is set to a chosen set-point value during the AFM scanning. With the same feedback value of A_1, the distance D may vary slightly at different locations of the cell because of the surface heterogeneity. The measured K_0'' is not sensitive to the small variations of D, as it is already saturated at small distances $D \ll D_c$, as shown in Fig. 3. Being operated at a resonant state, the long-needle AFM amplifies the signal and thus can accurately detect minute changes of the cell surface caused by an oscillatory draining flow in the nanoscale gap region.

To simplify the conversion of the AFM elastic map, we conduct a numerical analysis of Eq. (3) and find a simplified expression for

$$K_0'' \simeq \frac{6\pi\eta_0\omega R^2}{D_c}\,\tilde{p}(0;\alpha,\beta), \tag{4}$$

where

$$\tilde{p}(0;\alpha,\beta) \equiv \lim_{D\to 0}\frac{D_c}{D}\,\mathrm{Re}\left[\tilde{p}^*\left(\frac{D}{D_c};\alpha,\beta\right)\right] \tag{5}$$

is an analytical function of α and β with $\mathrm{Re}[\tilde{p}^*(D/D_c;\alpha,\beta)]$ being the real part of $\tilde{p}^*(D/D_c;\alpha,\beta)$. The analytical expression of $\tilde{p}(0;\alpha,\beta)$ is obtained at the small distance limit $D \ll D_c$, which allows us to directly compute the Young's modulus E at each location of the cell from the simultaneously measured values of the out-of-phase hydrodynamic response K_0'', resonant frequency ω_0, and cell height h, without involving the in-phase hydrodynamic response K' and complicated numerical solution of Eq. (3). Because the oscillating fiber is coupled to the elastic deformation of the cell surface through a draining flow in the gap region, there is a 90° phase change between the fiber oscillation and the response function $K^*(D)$ of the cell surface. As a result of this viscous coupling (as opposed to the elastic coupling by direct contact), the out-of-phase hydrodynamic response K_0'' is more closely connected to the cell's elasticity, instead of its viscosity.

To find the functional form of $\tilde{p}(0;\alpha,\beta)$, we first consider an elastic film of thickness h on a rigid substrate, which is immersed in a fluid of viscosity η_0, and a rigid spherical probe of radius R is placed at a distance D above the film and oscillates at a frequency ω. We apply the linear EHD theory [41] in the gap region as shown in the inset of Fig. 1 and find that the asymptotic value K_0'' in the small-D limit takes the form

$$K_0'' \sim \eta_0\omega R(E/\eta_0\omega)^{2/3}, \tag{6}$$

for large h and

$$K_0'' \sim \eta_0\omega R(R/h)(E/\eta_0\omega)^{1/3}, \tag{7}$$

for small h. The crossover between the two regimes occurs when the two quantities become equal with $(E/\eta_0\omega)^{1/3} = R/h$. We thus define a dimensionless parameter $\alpha = (h/R)(E/\eta_0\omega)^{1/3}$ to describe the elastic property of the cell. Similarly, we define another dimensionless parameter $\beta = (h/R)(E''/\eta_0\omega)^{1/3}$, with $E'' = 2(1+\nu)\eta\omega$ to describe the viscous property of the cell. We expect that K_0'' has a scaling form as shown in Eq. (4) for viscoelastic cells. When $\beta = 0$, Eq. (4) should recover to the pure elastic form with $\tilde{p}(0;\alpha \gg 1, 0) \simeq 1$ and $\tilde{p}(0;\alpha \ll 1, 0) \simeq 1/\alpha$, which are the proper asymptotic values of K_0'' in the two limiting cases.

Figure 4(a) shows the calculated $\tilde{p}(0;\alpha,\beta)$ as a function of α for different values of β (symbols) using the numerical solution of Eq. (3). In the numerical calculation, α is varied from 0.05 to 100 (3.5 decades) and β is varied from 0.2 to 20 (2 decades), in order to cover a wide range of viscoelasticity for living cells. The solid line shows the asymptotic expression of $\tilde{p}(0;\alpha,0)$ if the cell is purely elastic and its viscosity η can be ignored,

$$\tilde{p}(0;\alpha,0) \simeq n_0 + 6.05/\alpha, \tag{8}$$

where $n_0 = 1.163\,79$ is the asymptotic value of $\tilde{p}(0;\alpha,0)$ for a thick film ($\alpha \gg 1$). The second term on the right-hand side of Eq. (8) is the correction term for a thin film. Equation (8) agrees well with the numerical solution for $\beta = 0$ (black solid squares). Deviations from the solid line are found for different values of β, indicating that the hydrodynamic response function is indeed sensitive to the change of cell viscosity.

Figure 4(b) shows a scaling plot of $\tilde{p}(0;\alpha,\beta)[1 + 0.12(\beta/\alpha)^2]$ as a function of $\alpha/(1+0.2\beta)$. All the curves with different values of α and β collapse onto a single master curve in this plot. It is found that the universal scaling curve in Fig. 4(b) can be well described by the equation (solid line),

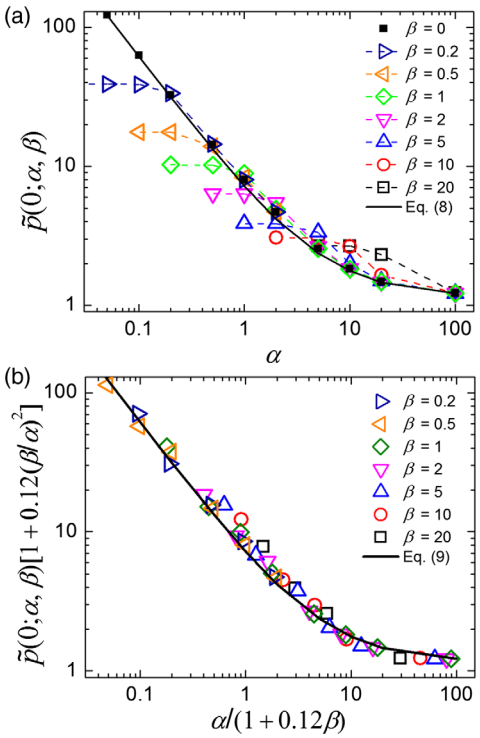

FIG. 4. (a) Calculated $\tilde{p}(0;\alpha,\beta)$ as a function of α for different values of β (color symbols) using the numerical solution of Eq. (3). The black solid line shows the analytical solution $\tilde{p}(0;\alpha,0)$ given in Eq. (8). (b) Scaling plot of $\tilde{p}(0;\alpha,\beta)[1+0.12(\beta/\alpha)^2]$ as a function of $\alpha/(1+0.2\beta)$. The data used are the same as those in (a). The black solid line is the analytical solution $\tilde{p}(0;\alpha,\beta)$ given in Eq. (9).

$$\tilde{p}(0;\alpha,\beta) \simeq \frac{n_0 + 6.05(1+0.12\beta)/\alpha}{1+0.12(\beta/\alpha)^2}. \quad (9)$$

When $\beta \to 0$, Eq. (9) recovers to Eq. (8) for a pure elastic film.

In the experiment, we find that while the Young's modulus E varies considerably at different positions on the cell surface, the viscosity η does not change much with the position. As shown in Fig. S2 of the Supplemental Material [46], the measured cell viscosity at two different locations does not show strong site dependence and is approximately 10 times larger than that of water. Therefore, we fix the value of η at 10 cP, which gives $\beta = (h/R)(3\eta/\eta_0)^{1/3} \simeq 3.11h/R$. With this fixed value of β, Eq. (4) becomes

$$K_0'' = \left(\frac{6\pi\eta_0\omega R^2}{D_c}\right)\frac{n_0 + 6.05(1+0.373h/R)/\alpha}{1+1.16[h/(R\alpha)]^2}. \quad (10)$$

In the above, there is only one unknown parameter α, which is directly linked to the Young's modulus $E = \eta_0\omega(\alpha R/h)^3$. Equation (10) is used for the conversion of the AFM elastic map.

V. ELASTIC MAPPING OF LIVING CELLS

Figure 5 shows the AFM images of a living Hela cell cultured in the DMEM buffer. The cell height image [Fig. 5(a)] and its three-dimensional (3D) plot [Fig. 5(e)] clearly reveal the cell boundary and topography. Detailed cell structures, such as lamellipodia and filopodia protrusions [pointed out by the arrow in Fig. 5(a)], are clearly observed. The cell height h varies from a fraction of microns near the boundary to about 4.5 μm at the center. The measured cell volume is $V \simeq 1.9 \times 10^3$ μm^3. The images of resonant frequency ω_0 [Fig. 5(c)] and dissipative force F_2 [Fig. 5(d)] show a clear contrast between the cell and collagen-coated coverslip substrate. The values of F_2 among different part of the cell vary in the range of 3–4 nN. This is a relatively weak force compared with the cell motility forces (~50 nN) [58], steric forces from the cell surface (~50 nN) [52,59], and forces used in other mechanical measurements (in the range of 1–200 nN) [16–18]. Therefore, the AFM-induced disturbances to the living cell will be minimal. Yet, FM mode AFM at the resonance is so sensitive to accurately detect F_2. Similarly, we conduct AFM imaging of Xenopus muscle

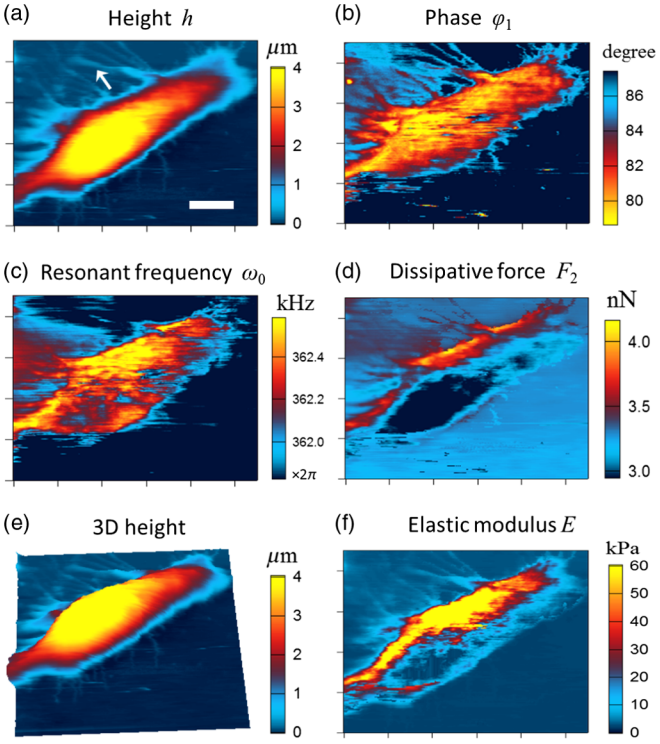

FIG. 5. AFM images of a living Hela cell. (a),(b) Images of cell height h and phase φ_1 obtained under the tapping mode. (c),(d) Images of resonant frequency ω_0 and dissipative force F_2 simultaneously obtained under the FM mode. (e) 3D height image converted from (a). (f) Image of Young's modulus E converted from images (a),(c),(d). The scale bar is 10 μm for all figures.

cells cultured in the phosphate-buffered saline buffer. The AFM images shown in Fig. S3 of the Supplemental Material [46] clearly reveal the surface texture and cytoskeletal bundles of the cell.

The image of Young's modulus E [Fig. 5(f)] is obtained using Eq. (10) together with the simultaneously measured values of F_2 [Fig. 5(d)], ω_0 [Fig. 5(c)], and h [Fig. 5(a)]. The measured values of E among different parts of the cell vary in the range of 10–80 kPa, which is a typical range of E reported in the previous single-point measurements of E on the cell [26]. Figures 5(f) and 5(a) reveal an important feature of this Hela cell, which is elastically polarized with larger values of E on the side with many protrusions than those on the other side of the cell. Lamellipodia and filopodia protrusions are known to be on the leading edge of the cell and play important roles in sensing and cell-to-cell interactions during the cell migration. This process involves an active polymerization of actin cytoskeleton on the leading edge of the cell [30,31], which can build up a gradient in actin concentration and thus lead to a polarization of the Young's modulus along the direction of cell migration.

VI. MECHANICAL CHANGES DURING THE CELL DIVISION

To further demonstrate the application of the long-needle AFM, we examine how the volumetric and elastic properties of a living cell change during the cell division. Figure 6 shows the optical (first row) and AFM (second and third rows) images of living Hela cells at four different stages of the cell division. The optical and AFM images are obtained simultaneously under the same cell conditions. It is seen that the AFM image of 3D cell height captures the same cell shape as the optical image does. The characteristic changes of cell morphology, as shown in Figs. 6(a)–6(d), are used as the hallmark to distinguish the different stages that the cell is at during the cell division.

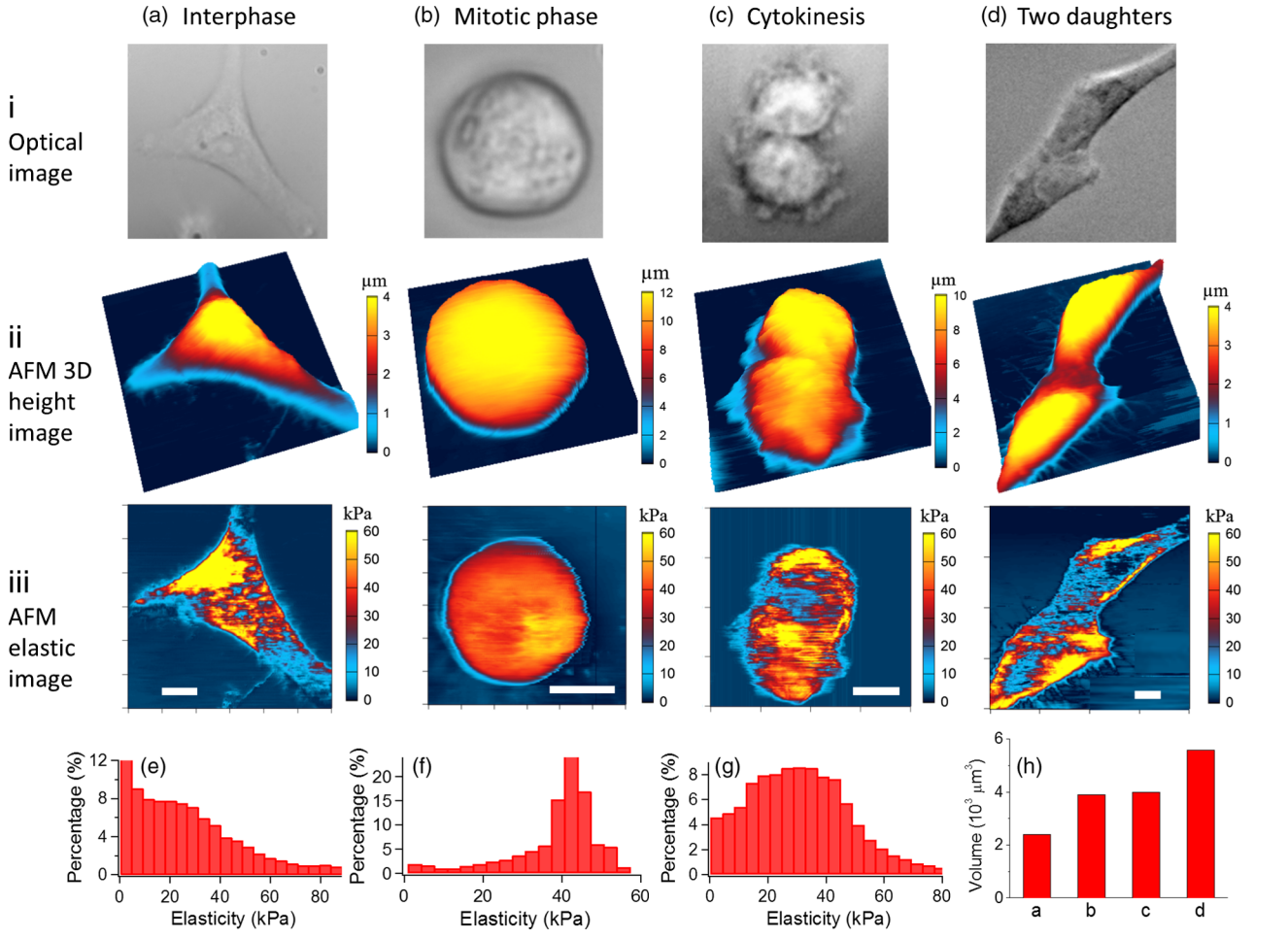

FIG. 6. Mechanical changes during the cell division. Optical image (first row) and AFM images of 3D height h (second row) and Young's modulus E (third row) of living Hela cells at four different stages of the cell division: interphase (a), mitosis (b), cytokinesis (c), and two daughter cells after division (d). (e)–(g) Histograms of the measured E in (a)(iii), (b)(iii), and (c)(iii), respectively. (h) Variations of the cell volume V at the four stages of the cell division. The scale bars are 10 μm.

Figure 6(a) (first column) shows the Hela cell in interphase before entering the mitotic phase. The cell spreads fully on the substrate, and its elastic map shows large spatial variations in the Young's modulus E. To further quantify the spatial heterogeneity of the elastic map, we plot, in Fig. 6(e), the histogram $H(E)$ of the measured E from different pixels. The obtained $H(E)$ in interphase shows a broad distribution with E varied in the range 10–80 kPa and mean value $\bar{E} \simeq 30$ kPa. It is a decaying function peaked at the lower end of E, indicating that most of the cell is soft.

Figure 6(b) (second column) shows that the Hela cell undergoes a significant morphology change from a highly spread state to a confined spherical shape, which is a hallmark of the cell entering the mitotic phase [32,33]. It is seen that the cell height is increased almost three times ($\sim$12 μm) compared with its value in interphase ($\sim$4 μm). It is found that the cell during the mitosis becomes mechanically stiffer and more homogenous. This finding is also quantitatively represented in the measured histogram $H(E)$, which shows a narrow distribution with a sharp peak at $\bar{E} \simeq 44$ kPa [Fig. 6(f)]. Recent studies of cell mitosis [32–35] suggested that the observed mitotic rounding and stiffening are associated with a profound structural change of the cortical actin network underneath the plasma membrane. The actin filaments in interphase form a branched outward-growing network capable of pushing the membrane to generate protrusions for cell spreading. When a cell enters mitosis, its actin filaments are aligned to form a dense network parallel to the plasma membrane, increasing the rigidity of the cortex and providing a support for cell division. Figure 6 thus demonstrates that the long-needle AFM is capable of providing quantitative information to further understand the interplay between the cell rounding, cortical stiffening, and cell adhesion weakening during the early stage of mitosis and find their correlations with the spindle formation and dynamics during mitosis [34,35].

Figure 6(c) (third column) shows the Hela cell in cytokinesis, in which the cytoplasm of the cell split up and two new cells begin to form with roughly equal shares of cellular components. The measured elastic map in cytokinesis shows the development of spacial heterogeneities, especially in the cleavage region, which appears softer than the rest of the cell. Compared with Fig. 6(f), the modulus peak of the measured $H(E)$ shown in Fig. 6(g) broadens while the peak height decreases and peak position shifts toward the lower values of E (i.e., becoming softer). As shown in Fig. 6(d) (fourth column), when the daughter cells enter interphase after the cell division, they acquire similar features as those shown in Fig. 6(a) [see Fig. S4 in the Supplemental Material [46] for the measured $H(E)$].

Figure 6(h) shows how the cell volume V changes during the cell division. The values of V are obtained by integrating the cell height images in the second row of Fig. 6. The volume of the Hela cell increases $\sim$50% when it enters the mitosis stage and remains unchanged during cytokinesis. The daughter cells continue to grow after the cell division and their total volume is finally doubled compared to the mother cell.

VII. SUMMARY

The above results clearly demonstrate that the long-needle AFM technique is a powerful tool for the study of evolution of the volumetric and elastic properties of a living cell during the cell division and differentiation. What is unique about the long-needle AFM is that it takes advantage of the useful features of the recently developed AFM methods and integrates them into a coherent design for high-quality and quantitative viscoelastic imaging of live cells. The noncontact dual-frequency imaging mode has a high spatial resolution down to 50–100 nm in a liquid medium, which allows us to observe several interesting features on a live cell surface, such as actin-filament bundles, lamellipodia protrusions, spatial variations, and polarization of the cell's elastic map, and evolution of the cell's elasticity during different stages of cell division. The simultaneous imaging of the cell's morphology and elasticity typically takes about 7 min to scan an area up to 90×90 μm^2 at the resolution of 256×256 pixels. This scanning speed thus allows one to conduct real-time AFM imaging of live cells under different biological conditions.

Like any promising AFM technique for live cell imaging, the long-needle AFM needs to be employed to a wide class of living cells under different sample situations. We find that good attachment of the cell to the substrate and a relatively clean surface of the cell without contaminating the scanning fiber tip by protein adsorption are two essential requirements for a better viscoelastic imaging of the living cells. With the combined quantitative information of the live cell's morphology, volume, and elastic modulus, one will be able gain insight into the major roles played by the cell's volumetric and mechanical properties and their response to external mechanical cues in regulating the essential cellular events and functions at an integrated molecular and cellular level.

ACKNOWLEDGMENTS

The authors wish to thank Dr. D. Beck, Dr. W. He, and Dr. L. Y. Zhou for useful discussions, and Dr. Y. Chen for providing the poly(L-lysine)-graft-poly(ethylene glycol) polymer sample. This work was supported in part by RGC of Hong Kong SAR under Grants No. T13-607/12R (R. Q. and P. T.) and No. AoE/P-02/12 (P. T.), and by Agence Nationale de la Recherche under Grant No. ANR-15-CE06-0005-02 (E. C.).

[1] D. E. Ingber, Tensegrity: The architectural basis of cellular mechanotransduction, Annu. Rev. Physiol. **59**, 575 (1997).

[2] V. Vogel and M. Sheetz, Local force and geometry sensing regulate cell functions, Nat. Rev. Mol. Cell Biol. **7**, 265 (2006).

[3] P. A. Janmey and C. A. McCulloch, Cell mechanics: Integrating cell responses to mechanical stimuli, Annu. Rev. Biomed. Eng. **9**, 1 (2007).

[4] P. P. Girard, E. A. Cavalcanti-Adam, R. Kemkemer, and J. P. Spatz, Cellular chemomechanics at interfaces: Sensing, integration and response, Soft Matter **3**, 307 (2007).

[5] K. E. Kasza, A. C. Rowat, J. Liu, T. E Angelini, C. P. Brangwynne, G. H. Koenderink, and D. A. Weitz, The cell as a material, Curr. Opin. Chem. Biol. **19**, 101 (2007).

[6] E. Moeendarbary and A. R. Harris, Cell mechanics: Principles, practices, and prospects, WIREs Syst. Biol. Med. **6**, 371 (2014).

[7] M. Lekka, P. Laidler, D. Gil, J. Lekki, Z. Stachura, and A. Z. Hrynkiewicz, Elasticity of normal and cancerous human bladder cells studied by scanning force microscopy, Eur. Biophys. J. **28**, 312 (1999).

[8] M. Nagayama, H. Haga, and K. Kawabata, Drastic change of local stiffness distribution correlating to cell migration in living fibroblasts, Cell Motil. Cytoskeleton **50**, 173 (2001).

[9] B. Fabry, G. N. Maksym, J. P. Butler, M. Glogauer, D. Navajas, and J. J. Fredberg, Scaling the Microrheology of Living Cells, Phys. Rev. Lett. **87**, 148102 (2001).

[10] D. T. Chen, E. R. Weeks, J. C. Crocker, M. F. Islam, R. Verma, J. Gruber, A. J. Levine, T. C. Lubensky, and A. G. Yodh, Rheological Microscopy: Local Mechanical Properties from Microrheology, Phys. Rev. Lett. **90**, 108301 (2003).

[11] M. L. Gardel, M. T. Valentine, J. C. Crocker, A. R. Bausch, and D. A. Weitz, Microrheology of Entangled F-Actin Solutions, Phys. Rev. Lett. **91**, 158302 (2003).

[12] D. A. Fletcher and R. D. Mullins, Cell mechanics and the cytoskeleton, Nature (London) **463**, 485 (2010).

[13] X. Wang and T. Ha, Defining single molecular forces required to activate integrin and notch signaling, Science **340**, 991 (2013).

[14] E. Moeendarbary, L. Valon, M. Fritzsche, A. R. Harris, D. A. Moulding, A. J. Thrasher, E. Stride, L. Mahadevan, and G. T. Charras, The cytoplasm of living cells behaves as a poroelastic material, Nat. Mater. **12**, 253 (2013).

[15] R. M. Hochmuth, Micropipette aspiration of living cells, J. Biomech. **33**, 15 (2000).

[16] D. Sánchez *et al.*, Noncontact measurement of the local mechanical properties of living cells using pressure applied via a pipette, Biophys. J. **95**, 3017 (2008).

[17] O. Thoumine and A. Ott, Time scale dependent viscoelastic and contractile regimes in fibroblasts probed by microplate manipulation, J. Cell Sci. **110**, 2109 (1997).

[18] I. Sokolov, M. E. Dokukin, and N. V. Guz, Method for quantitative measurements of the elastic modulus of biological cells in AFM indentation experiments, Methods **60**, 202 (2013).

[19] Y. Shen, D. Guan, D. Serien, S. Takeuchi, P. Tong, L. Yobas, and P. Huang, Mechanical characterization of microengineered epithelial cysts by using atomic force microscopy, Biophys. J. **112**, 398 (2017).

[20] F. Amblard, A. C. Maggs, B. Yurke, A. N. Pargellis, and S. Leibler, Subdiffusion and Anomalous Local Viscoelasticity in Actin Networks, Phys. Rev. Lett. **77**, 4470 (1996).

[21] J. Dai and M. Sheetz, Mechanical properties of neuronal growth cone membranes studied by tether formation with laser optical tweezers, Biophys. J. **68**, 988 (1995).

[22] D. Weihs, T. G. Mason, and M. A. Teitell, Bio-microrheology: A frontier in microrheology, Biophys. J. **91**, 4296 (2006).

[23] B. D. Hoffman, G. Massiera, K. M. Van Citters, and J. C. Crocker, The consensus mechanics of cultured mammalian cells, Proc. Natl. Acad. Sci. U.S.A. **103**, 10259 (2006).

[24] M. J. Higgins, T. Fukuma, and S. P. Jarvis, AFM in liquid: A high sensitivity study on biological membranes, Imaging Microsc. **8**, 47 (2006).

[25] D. J. Müller and Y. F. Dufréne, Atomic force microscopy: A nanoscopic window on the cell surface, Trends Cell Biol. **21**, 461 (2011).

[26] T. G. Kuznetsova, M. N. Starodubtseva, N. I. Yegorenkov, S. A. Chizhik, and R. I. Zhdanov, Atomic force microscopy probing of cell elasticity, Micron **38**, 824 (2007).

[27] A. Raman, S. Trigueros, A. Cartagena, A. P. Z. Stevenson, M. Susilo, E. Nauman, and S. Antoranz Contera, Mapping nanomechanical properties of live cells using multi-harmonic atomic force microscopy, Nat. Nanotechnol. **6**, 809 (2011).

[28] P. Hinterdorfer and Y. F. Dufréne, Detection and localization of single molecular recognition events using atomic force microscopy, Nat. Methods **3**, 347 (2006).

[29] R. Matzke, K. Jacobson, and M. Radmacher, Direct, high-resolution measurement of furrow stiffening during division of adherent cells, Nat. Cell Biol. **3**, 607 (2001).

[30] P. K. Mattila and P. Lappalainen, Filopodia: Molecular architecture and cellular functions, Nat. Rev. Mol. Cell Biol. **9**, 446 (2008).

[31] R. Li and G. G. Gundersen, Beyond polymer polarity: How the cytoskeleton builds a polarized cell, Nat. Rev. Mol. Cell Biol. **9**, 860 (2008).

[32] P. Kunda, A. E. Pelling, T. Liu, and B. Baum, Moesin controls cortical rigidity, cell rounding, and spindle morphogenesis during mitosis, Curr. Biol. **18**, 91 (2008).

[33] M. P. Stewart, J. Helenius, Y. Toyoda, S. P. Ramanathan, D. J. Muller, and A. A. Hyman, Hydrostatic pressure and the actomyosin cortex drive mitotic cell rounding, Nature (London) **469**, 226 (2011).

[34] P. Kunda and B. Baum, The actin cytoskeleton in spindle assembly and positioning, Trends Cell Biol. **19**, 174 (2009).

[35] O. M. Lancaster and B. Baum, Shaping up to divide: Coordinating actin and microtubule cytoskeletal remodelling during mitosis, Semin. Cell Dev. Biol. **34**, 109 (2014).

[36] Y. Naitoh, Z. Ma, Y. J. Li, M. Kageshima, and Y. Sugawara, Simultaneous observation of surface topography and elasticity at atomic scale by multifrequency frequency modulation atomic force microscopy, J. Vac. Sci. Technol. B **28**, 1210 (2010).

[37] R, Garcia, and R Proksch, Nanomechanical mapping of soft matter by bimodal force microscopy, Eur. Polym. J. **49**, 1897 (2013).

[38] M. Minary-Jolandan, A. Tajik, N. Wang, and M.-F. Yu, Intrinsically high-Q dynamic AFM imaging in liquid with a significantly extended needle tip, Nanotechnology **23**, 235704 (2012).

[39] J. Rheinlaender and T. E. Schaffer, Mapping the mechanical stiffness of live cells with the scanning ion conductance microscope, Soft Matter **9**, 3230 (2013).
[40] Y.-S. Chu, S. Dufour, J. P. Thiery, E. Perez, and F. Pincet, Johnson-Kendall-Roberts Theory Applied to Living Cells, Phys. Rev. Lett. **94**, 028102 (2005).
[41] S. Leroy and E. Charlaix, Hydrodynamic interactions for the measurement of thin film elastic properties, J. Fluid Mech. **674**, 389 (2011).
[42] S. Leroy, A. Steinberger, C. Cottin-Bizonne, F. Restagno, L. Leger, and E. Charlaix, Hydrodynamic Interaction between a Spherical Particle and an Elastic Surface: A Gentle Probe for Soft Thin Films, Phys. Rev. Lett. **108**, 264501 (2012).
[43] X. Xiong, S. Guo, Z. Xu, P. Sheng, and P. Tong, Development of an atomic-force-microscope-based hanging-fiber rheometer for interfacial microrheology, Phys. Rev. E **80**, 061604 (2009).
[44] S. Guo, M. Gao, X. Xiong, Y. J. Wang, X. Wang, P. Sheng, and P. Tong, Direct Measurement of Friction of a Fluctuating Contact Line, Phys. Rev. Lett. **111**, 026101 (2013).
[45] J. D. de Baubigny, M. Benzaquen, L. Fabié, M. Delmas, J.-P. Aimé, M. Legros, and T. Ondarçuhu, Shape and effective spring constant of liquid interfaces probed at the nanometer scale: Finite size effects, Langmuir **31**, 9790 (2015).
[46] See Supplemental Material at http://link.aps.org/supplemental/10.1103/PhysRevApplied.8.044010 for more details about the supplemental figures, methods, and discussion, which includes Refs. [47,48].
[47] S. Guo, X.-M. Xiong, Z.-L. Xu, P. Sheng, and P. Tong, Measurement of the friction coefficient of a fluctuating contact line using an AFM-based dual-mode mechanical resonator, Chin. Phys. B **23**, 116802 (2014).
[48] N. Gavara and R. S. Chadwick, Determination of the elastic moduli of thin samples and adherent cells using conical atomic force microscope tips, Nat. Nanotechnol. **7**, 733 (2012).
[49] B. Pidhatika M. Rodenstein, Y. Chen, E. Rakhmatullina, A. Mühlebach, C. Acikgöz, M. Textor, and R. Konradi, Comparative stability studies of poly(2-methyl-2-oxazoline) and poly(ethylene glycol) brush coatings, Biointerphases **7**, 1 (2012).
[50] D. Guan, Z. H. Hang, Z. Marcet, H. Liu, I. I. Kravchenko, C. T. Chan, H. B. Chan, and P. Tong, Direct measurement of optical force induced by near-field plasmonic cavity using dynamic mode AFM, Sci. Rep. **5**, 16216 (2015).
[51] D. Y. C. Chan and R. G. Horn, The drainage of thin liquid films between solid surfaces, J. Chem. Phys. **83**, 5311 (1985).
[52] S. Iyer, R. M. Gaikwad, V. Subba-Rao, C. D. Woodworth, and I. Sokolov, Atomic force microscopy detects differences in the surface brush of normal and cancerous cells, Nat. Nanotechnol. **4**, 389 (2009).
[53] D. Guan, C. Barraud, E. Charlaix, and P. Tong, Noncontact viscoelastic measurement of thin polymer films in a liquid medium using long-needle atomic force microscopy, Langmuir **33**, 1385 (2017).
[54] D. Guan, Y. J. Wang, E. Charlaix, and P. Tong, Asymmetric and Speed-Dependent Capillary Force Hysteresis and Relaxation of a Suddenly Stopped Moving Contact Line, Phys. Rev. Lett. **116**, 066102 (2016).
[55] Y. J. Wang, S. Guo, H.-Y. Chen, and P. Tong, Understanding contact angle hysteresis on an ambient solid surface, Phys. Rev. E **93**, 052802 (2016).
[56] H. Brenner, The slow motion of a sphere through a viscous fluid towards a plane surface, Chem. Eng. Sci. **16**, 242 (1961).
[57] Y. Hu, X. Chen, G. M. Whitesides, J. J. Vlassak, and Z. Suo, Indentation of polydimethylsiloxane submerged in organic solvents, J. Mater. Res. **26**, 785 (2011).
[58] R. Ananthakrishnan and A. Ehrlicher, The forces behind cell movement, Int. J. Biol. Sci. **3**, 303 (2007).
[59] H.-J. Butt, M. Kappl, H. Mueller, R. Raiteri, W. Meyer, and J. Rühe, Steric forces measured with the atomic force microscope at various temperatures, Langmuir **15**, 2559 (1999).